JOURNAL OF GEOPHYSICAL RESEARCH, VOL. 107, NO. A11, 1413, doi:10.1029/2002JA009272, 2002

Electron acceleration in the ionospheric Alfven resonator

C. C. Chaston, J. W. Bonnell, C. W. Carlson, M. Berthomier, L. M. Peticolas, I. Roth, and J. P. McFadden

Space Sciences Laboratory, University of California, Berkeley, California, USA

R. E. Ergun

Laboratory for Atmospheric and Space Physics, University of Colorado, Boulder, Colorado, USA

R. J. Strangeway

Institute of Geophysics and Planetary Physics, University of California, Los Angeles, California, USA

Received 21 January 2002; revised 21 June 2002; accepted 13 August 2002; published 29 November 2002.

[1] FAST wave and particle observations on the nightside polar cap boundary indicate the operation of the ionospheric Alfven resonator (IAR). Large impulsive electric and magnetic field deviations on the boundary between the auroral oval and the polar cap close to magnetic midnight are correlated with accelerated electrons and excite semi periodic oscillations with a frequency of ~0.5 Hz. Linear one-dimensional simulations of the Alfven resonator including parallel electric fields due to electron inertial effects, the ionospheric feedback instability and statistically determined altitude dependent density and composition profiles in a dipole geomagnetic field yield waveforms and electron energy spectra qualitatively similar to observations. However, from comparison with a case study example observed above a sunlit ionosphere, the observed electron energies (which exceed 10 keV) suggest that the observed wave carries a parallel electric field larger than possible from electron inertial effects in the linear approximation particularly if this acceleration occurs at altitudes within the ionospheric Alfven resonator. *INDEX TERMS:* 2752 Magnetospheric Physics: MHD waves and instabilities; 2716 Magnetospheric Physics: Energetic particles, precipitating; 2483 Ionosphere: Wave/particle interactions; 2712 Magnetospheric Physics: Electric fields (2411); *KEYWORDS:* Alfven waves, electron acceleration, aurora, magnetohydrodynamics, kinetic effects, ionospheric Alfven resonator

Citation: Chaston, C. C., J. W. Bonnell, C. W. Carlson, M. Berthomier, L. M. Peticolas, I. Roth, J. P. McFadden, R. E. Ergun, and R. J. Strangeway, Electron acceleration in the ionospheric Alfven resonator, *J. Geophys. Res.*, *107*(A11), 1413, doi:10.1029/2002JA009272, 2002.

1. Introduction

[2] The transition in altitude from magnetospheric to ionospheric plasma above the auroral oval is not smooth. The rapid increase in plasma mass density that occurs at altitudes below ~1 Earth radius results in strong gradients in the Alfven speed and the formation of a resonant cavity for Alfven waves. This cavity has been termed the ionospheric Alfven resonator (IAR) [*Trakhtengertz and Feldstein*, 1987; *Lysak*, 1988; *Pokhotelov et al.*, 2000]. In this region, Alfven waves may reflect between the conducting ionosphere and the strong gradients in Alfven speed above the ionosphere to an extent dependent on the reflection coefficients at these boundaries [*Lysak*, 1991; *Lessard and Knudsen*, 2001]. At perpendicular scales of the order of an electron skin-depth (or electron inertial length $c/\omega_{pe} = \lambda_e$ where ω_{pe} is the electron plasma frequency) or less these waves carry a parallel wave electric field and may cause electron acceleration [*Goertz and Boswell*, 1979]. It is the intent of this report to examine the ability of inertial Alfven waves in the IAR cavity and at altitudes above to accelerate electrons.

[3] While there exist a large number of observations from the ground of the operation of the IAR [*Belyaev et al.*, 1999] there have been relatively few reports of its observation in situ [*Grzesiak*, 2000]. This has been the case since low-altitude spacecraft pass so quickly through the IAR cavity that resonant structure is difficult to resolve. Nonetheless, there is a significant amount of literature devoted to the description of Alfvenic fluctuations at IAR altitudes above the auroral oval [*Boehm et al.*, 1990; *Louarn et al.*, 1994; *Knudsen et al.*, 1992; *Chaston et al.*, 1999]. However, since these waves have usually been spatially localized consisting of 1–2 cycles at the lowest frequencies, identification of the expected phase relationships between electric and magnetic field has proved difficult. Most recently, *Grzesiak* [2000] has used the wavelet transform to show similarity between the predicted frequency dependent phase difference of electric and magnetic field fluctuations [*Lysak*, 1991] and that observed from Freja.

0148-0227/02/2002JA009272$09.00

[4] In the auroral acceleration region the electron thermal speed can be much less than the local Alfven speed so that ideal MHD wave dispersion is significantly modified by the effects of electron inertia. Such a wave is usually called an inertial Alfven wave, which in the local approximation has the dispersion relation

$$\frac{\omega}{k_\parallel} = \frac{V_A}{\sqrt{1 + k_\perp^2 \lambda_e^2}}, \tag{1}$$

has an electric to magnetic field amplitude related by

$$\frac{E_{\perp 1}}{B_{\perp 2}} = V_A \sqrt{1 + k_\perp^2 \lambda_e^2} \tag{2}$$

and carries a parallel electric field amplitude given by

$$\frac{E_\parallel}{E_{\perp 1}} = \frac{k_\parallel k_\perp \lambda_e^2}{1 + k_\perp^2 \lambda_e^2}, \tag{3}$$

where V_A is the local Alfven speed, $E_{\perp 1}$ is the wave electric field amplitude measured perpendicular to the geomagnetic field, $B_{\perp 2}$ is the wave magnetic field amplitude measured perpendicular to the geomagnetic field and $E_{\perp 1}$, and $k_\perp$ is the perpendicular wave number of the Alfven wave. The result that such a wave carries a parallel electric field and that large amplitude electromagnetic waves with $E_{\perp 1}/B_{\perp 1} \sim V_A$ and $k_\perp \lambda_e \sim 1$ are observed from rockets and low-altitude spacecraft [*Stasiewicz et al.*, 2000] has motivated a number of studies [*Goertz and Boswell*, 1979; *Kletzing*, 1994; *Hui and Seyler*, 1993; *Clark and Seyler*, 1999; *Kletzing and Hu*, 2001] to examine the ability of such waves to accelerate electrons. In this report we extend the work of *Chaston et al.* [2000, 2002b] to compare observations of wave fields and accelerated electron distributions associated with Alfven waves in the IAR with the predictions of a linear MHD simulation [*Thompson and Lysak*, 1996] modified to include the ionospheric feedback instability [*Lysak*, 1991]. The model incorporates the important macroscopic features of the plasma above the auroral oval as well as the microscopic effects of electron inertia along auroral geomagnetic fieldlines from 100 km up to 5 Earth radii in altitude.

[5] In this paper we first present an example of FAST observations of the ionospheric Alfven resonator. We then develop the simulation model and compare the simulation results with the observations.

2. Ionospheric Alfven Resonator Case Study

[6] Figure 1a shows observations from the FAST spacecraft as it skimmed along the boundary between the polar cap and high-latitude auroral oval in the Northern Hemisphere. At this time the entire statistical auroral oval was in daylight. The first panel shows the electric field measured along the spacecraft trajectory and consists of semi-periodic oscillations with frequency of the order of ~1 Hz. The magnetic

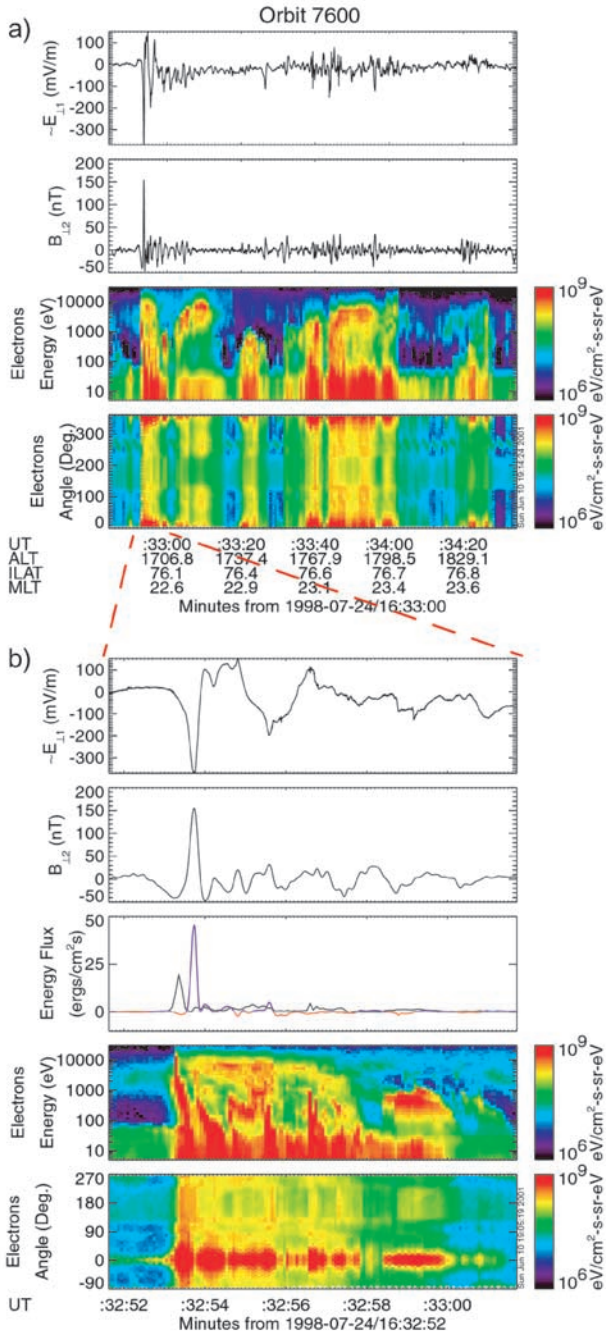

Figure 1. (opposite) FAST observations of the ionospheric resonator at the polar cap boundary. The first panel in Figure 1a shows the electric field ($E_{\perp 1}$) measured perpendicular to the geomagnetic field (B_o) and along the spacecraft trajectory, the second panel shows the wave magnetic field ($B_{\perp 2}$) measured perpendicular to $E_{\perp 1}$ and B_o, and the third and fourth panel show the electron energy and pitch angle spectra measured in this region. (b) A "zoom-in" on the impulsive wave activity on the far left of Figure 1a showing the wave fields, $E_{\perp 1}$ and $B_{\perp 2}$, in the first two panels and the wave Poynting flux in the third panel with blue indicating downward (positive) and red upwards (negative) propagation. The black trace in this panel is the integrated electron energy flux which is everywhere downward in this plot. The lowest two panels in Figure 1b are high-resolution electron energy and pitch angle spectra measured coincident with the wave activity.

field time series in the next panel is well correlated with the electric field. The third and fourth panels of this figure show the electron energy and pitch angle spectra revealing a somewhat bursty nature with enhanced field-aligned fluxes (0° in panel 4) coincident with the larger amplitude field fluctuations. The most prominent is on the far left of these two panels at 1632:40 UT where there is an abrupt enhancement in energy flux particularly in the field-aligned direction coincident with a large impulsive deviation in the electric and magnetic time series. The fine structure in this field-aligned burst is revealed in Figure 1b.

[7] The first two panels of Figure 1b show a large amplitude gaussian-like pulse starting at 1632:53.5 UT with full width at half maximum of ~ 0.5 s in $E_{\perp 1}$ and $B_{\perp 2}$. The two measurements are separated in phase by π radians as expected for a traveling electromagnetic wave. Subsequent to the pulse there are oscillations at several characteristic frequencies with amplitudes that decay in time from left to right in the figure. The third panel shows the wave Poynting flux (purple and red) and downgoing electron energy flux (black). The Poynting flux shows a clear downgoing (positive-purple) spike associated with the initial field pulse consistent with a traveling wave and then comparatively smaller upgoing (red) and downgoing fluxes, perhaps representing a standing wave. The electron energy flux shown in the same panel shows the same basic pattern except that the net electron energy flux is always downward. The peak in the electron energy flux at 1632:53.3 UT precedes the arrival of the wave Poynting flux at spacecraft altitudes suggesting that if the wave has resonantly accelerated these electrons at some higher altitude, then it has slowed down between acceleration region and the spacecraft while the electrons have continued earthward at the resonant speed. Significantly, the wave Poynting flux at this altitude is about twice the size of the electron energy flux.

[8] The energy spectra shown in the fourth panel shows several dispersive electron bursts with the first extending to energies up to 10 keV and preceding the field pulse. Calculation of a source altitude for the precipitating electrons in the first burst at energies above 100 eV suggests that they are accelerated from ~5000 km. The subsequent bursts begin at progressively smaller energies with slower dispersion. At energies below 100 eV there is almost no dispersion suggesting near local acceleration. The fifth panel shows that the bursts are field-aligned and predominately downgoing and within the source cone (i.e., that range of pitch angles containing electrons which will be lost to the atmosphere). There are at times enhancements in the upgoing electrons (180°) representing backscattered fluxes from the ionosphere and perhaps field-aligned acceleration in the upward direction. The isotropic fluxes observed throughout are plasma sheet electrons. These are hotter than typical plasma sheet electrons observed from FAST and have a temperature of the order of a few keV. (In fact, the plasma sheet ion temperature at this time is in excess of 10 keV.)

[9] A simple way to verify that the field observations are consistent with the operation of the IAR is to calculate the relative phasing between $E_{\perp 1}$ and $B_{\perp 2}$ as a function of frequency using cross-spectral techniques. This is the same approach adopted by *Grzesiak* [2000], who use the wavelet transform. We however find the Fourier transform approach sufficient and the results of this analysis are presented in Figure 2, which shows that the wave fields are consistent with the operation of a weak resonator. Figure 2a shows the wave power spectra in $E_{\perp 1}$ (solid line) and $B_{\perp 2}$ (dashed line) averaged over the interval contained in Figure 1b. The electric and magnetic field spectra are peaked at 0.5 Hz and 0.75 Hz, respectively, corresponding to the lowest-frequency oscillations visible in the time series shown in Figure 1b. At higher frequencies it is difficult to identify any distinct features and both roughly obey power laws. Figure 2b shows that variations in $E_{\perp 1}$ and $B_{\perp 2}$ are highly coherent at frequencies below 4 Hz, allowing us to perform a reliable cross-phase calculation between the two components. The results of this calculation are presented in Figure 2c. Below 4 Hz the phase difference is oscillatory about +/− π with a periodicity in frequency of ~1 Hz, indicating the excitation of

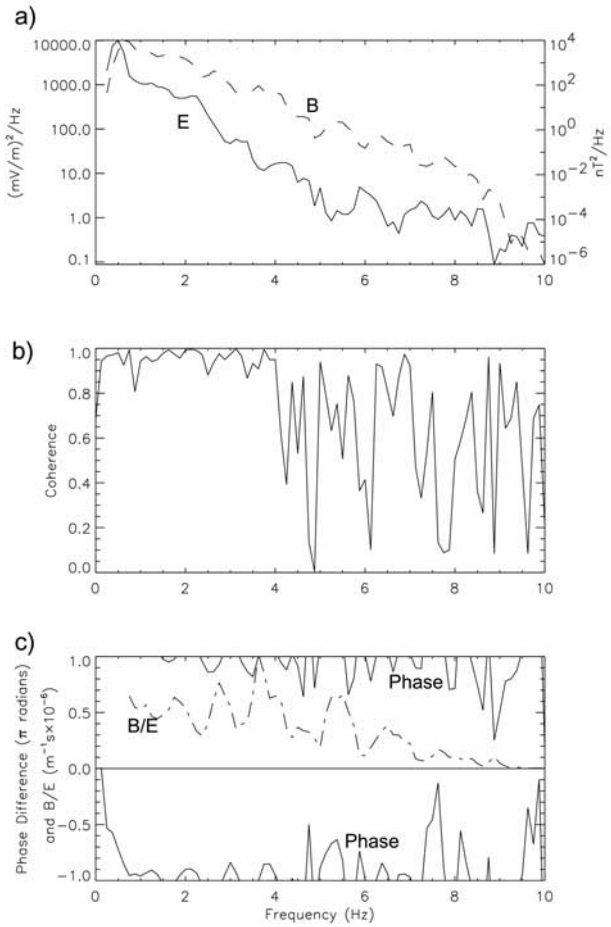

Figure 2. Spectral structure of the observed wave fields inside the resonator shown in Figure 1b). (a) The wave power spectra from $E_{\perp 1}$ (solid line) and $B_{\perp 2}$ (dashed line). Peak spectral energy density is at 0.5 Hz in $E_{\perp 1}$ and 0.75 Hz in $B_{\perp 2}$. (b) The spectral coherency of the wave fields with a value of 1 indicating a constant phase difference between $E_{\perp 1}$ and $B_{\perp 1}$ over the event window. (c) The phase of $E_{\perp 1}$ relative to $B_{\perp 1}$ (solid line) and the value of the ratio $B_{\perp 1}/E_{\perp 1}$ (dashed line) times 10^6 m^{-1} s.

the several harmonics of the resonator. Above 4 Hz the coherency varies, making the results somewhat less reliable; however, a similar pattern in phase persists. This is the pattern expected for the IAR as demonstrated by *Lysak* [1991]. For a traveling wave the expected phase difference is +/− π, while for a standing wave the expected phase difference is +/− π/2. The observed oscillation in phase with frequency is due to the changing nature of the wave field between these limits as the frequency passes through the harmonics of the resonator fundamental frequency at $\sim n \times 1$ Hz. The fact that the phase difference throughout remains close to +/− π indicates a weak resonance with most of the observed wave power traveling through the boundaries of the resonator without reflection to yield the observed decaying of the field amplitudes in time. The dashed-dotted line in Figure 2c shows the frequency dependent $B_{\perp 2}/E_{\perp 1}$ ratio modulated in the manner expected for the IAR [*Lysak*, 1991] where nodes in $E_{\perp 1}$ and $B_{\perp 2}$ are anticorrelated.

[10] In summary the observations show an impulsive wave field followed by oscillations with decreasing amplitude in time and phasing as expected for a weak ionospheric resonator. This wave field is coincident with a number of dispersive electron bursts with decreasing peak energy and increasing dispersion times subsequent to the initial field perturbation. We now attempt to explain these observations by simulating the wave fields and electron acceleration using a linear one-dimensional inertial MHD code and test electrons.

3. Wave Propagation

3.1. Wave Model

[11] We model these observations by launching an Alfven wave from a perturbation in the parallel potential from an altitude of 30000 km. The wave field is determined as function of time and altitude in one dimension along the field line according to the model equations from *Thompson and Lysak* [1996], which are in SI units,

$$\frac{V_A^2}{1+\left(V_A^2/c^2\right)}\cdot\frac{\partial A_z(z,t)}{\partial z}+\frac{\partial \Phi_w(z,t)}{\partial t}=0 \tag{4}$$

$$\left(1+k_\perp^2\lambda_e^2\right)\cdot\frac{\partial A_z(z,t)}{\partial t}+\frac{\partial \Phi_w(z,t)}{\partial z}=0, \tag{5}$$

where $A_z(z,t)$ is the vector potential, $\Phi_w(z,t)$ is the wave scalar potential, $V_A^2/(1 + V_A^2/c^2)$ is the Alfven speed with a relativistic correction necessary in low-density regions, and z is a coordinate representing the altitude with t being time. We have Fourier transformed in the x-direction (north-south) and assumed uniformity in the y-direction (East-West). As a result the field variations perpendicular to the geomagnetic field (x-direction) are periodic with $k_\perp$ and are given by $E_{\perp 1}(x,z,t) = E_{\perp 1}(0,z,t)\cos(k_\perp x)$ and $B_{\perp 2}(x,z,t) = B_{\perp 2}(0,z,t)\cos(k_\perp x)$ where $E_{\perp 1}(0,z,t) = k_\perp(z)\Phi_w(z,t)$ and $B_{\perp 2}(0,z,t) = k_\perp(z)A_z(z,t)$. Equations (4) and (5) are solved using a standard leapfrog technique (for the reasons described by *Thompson and Lysak* [1996]) subject to appropriate boundary conditions at the ionospheric and magnetospheric ends.

[12] The boundary condition at the ionospheric end of the simulation is provided by current continuity. After *Lysak* [1990; equation (20)] this yields the field-aligned current out of the ionosphere, j_z, as

$$j_z = \Sigma_p\nabla_\perp^2\Phi + \nabla_\perp\Sigma_p \bullet \nabla_\perp\Phi - (\nabla_\perp\Sigma_H \times \nabla_\perp\Phi)\bullet\hat{z}, \tag{6}$$

where Σ_P and Σ_H are the height-integrated Pedersen and Hall conductivities, respectively, and $\nabla_\perp$ is the gradient operator in the direction perpendicular to $\mathbf{B}_o$. $\Phi = \Phi_C + \Phi_w$ is the scalar potential in the ionosphere and includes contributions from ionospheric convection, Φ_C, and the wave scalar potential, Φ_w. The field-aligned current carried by the wave is given by Ampere's law, $j_z = (1/\mu_o).(\nabla \times \mathbf{B})_z$, and so using $\mathbf{B} = \nabla \times \mathbf{A}$ the Fourier transform yields, $j_z = (k_\perp^2 A_z)/\mu_o$. Hence in the case of uniform ionospheric conductivity, where only first term on the right side of equation (6) survives, we obtain the boundary condition, $A_z + \mu_0\Sigma_P\Phi_w = 0$ as used previously by *Thompson and Lysak* [1996] and *Chaston et al.* [2000, 2002b]. To incorporate the feedback instability we instead assume that the height integrated conductivity can be linearized and Fourier transformed perpendicular to $\mathbf{B}_o$ as $\Sigma_P = \Sigma_{Po} + \Sigma_{P1}$ and $\Sigma_H = \Sigma_{Ho} + \Sigma_{H1}$ were $\Sigma_1 = \Sigma_1(t)\exp(ik_\perp x)$. Substituting this expression for Σ_P into equation (6) yields the new boundary condition at the ionosphere

$$A_z + \mu_o\Sigma_{po}\Phi + i\mu_o\Sigma_{P1}\frac{\hat{k}_\perp}{k_\perp}\bullet E_o - i\mu_o\Sigma_{H1}\frac{\hat{k}_\perp}{k_\perp}\times E_o = 0, \tag{7}$$

where $\mathbf{E}_o$ is the convection electric field in the ionosphere and $\hat{k}_\perp$ is a unit vector in the $\mathbf{k}_\perp$ direction.

[13] To implement this boundary condition the temporal variation in $\Sigma_{P1,\ H1}$ is related to the thermal current carried by the wave in the same way as performed by *Lysak* [1991]. In this approach the height integrated conductivity is assumed proportional to the ionospheric density so that $\Sigma_P = \mathrm{P}n = P(n_o + n_1)$ and $\Sigma_H = Hn = H(n_o + n_1)$. The ionospheric density obeys a continuity equation given by

$$\left(\frac{\partial}{\partial t} + v_o \bullet \nabla_\perp\right)n = S - R\left(n^2 - n_o^2\right), \tag{8}$$

where S is a source term and R is the recombination coefficient and $\mathbf{v}_o = \mathbf{E}_o \times \mathbf{B}_o/B_o^2$. If S is proportional to the field aligned current density, j_z, then we can write $S = Q \cdot (k_\perp^2 A_z)/\mu_o$. If each incident electron produces γ electrons in the ionosphere, then $Q = \gamma/(e\Delta_z)$, where Δ_z is the thickness of the current carrying region of the ionosphere. Substituting equation (8) we obtain

$$\left(\frac{\partial}{\partial t} + iv_o \bullet k_\perp\right)n_1 = Qk_\perp^2 A_z/\mu_o - R\left(2n_o n_1 + n_1^2\right), \tag{9}$$

where we have retained the second order term on the left, n_1^2, because n_1 can easily be as large as n_o. The magnitude of n_1 is however limited by the spatial Fourier transform that requires the magnitude of n_1 be less than n_o, since n cannot be negative. This is a nonphysical constraint since in the nonlinear case conductivity enhancements (and so densities) an order of magnitude larger then the equilibrium value occur [*Lysak*, 1986] and are in fact observed [*Kelley et al.*, 1982]. For the purposes of this case study, however, it will be seen that the linear result is adequate.

[14] Equation (9) is solved for n_1 at each time step using a standard fourth-order Runge-Kutta technique. This then

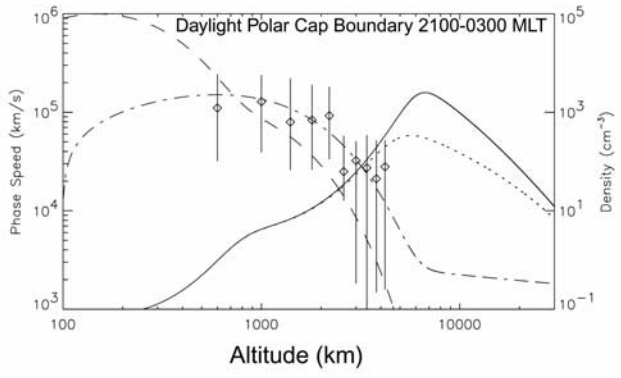

Figure 3. Altitude dependent density and composition profile for the sunlit polar cap boundary layer near midnight. The dashed line and the dot-dashed line are the O^+ and H^+ densities, respectively. The solid line is the Alfven speed and the dotted line is the inertial Alfven speed for a perpendicular wavelength in the ionosphere of 5 km. The diamonds are observations of electron density from the FAST spacecraft with error bars indicating the range of values observed at each altitude.

provides the necessary input for the application of the ionospheric boundary condition given by equation (7).

[15] At the magnetospheric end we allow the wave to travel freely through the boundary without reflection. The appropriate boundary condition in this case follows directly from *Thompson and Lysak* [1996] and is

$$A_z + \mu_0 \Sigma_A \Phi_o(t) = \mu_o \Sigma_A \Phi, \tag{10}$$

where Σ_A is the Alfven conductivity given by $\Sigma_A = 1/[\mu_0(V_A/(1 + V_A^2/c^2)^{1/2} \cdot (1 + k_\perp^2\lambda_e^2)^{1/2}]$ and $\Phi_o(t)$ is the applied gaussian potential variation at the magnetospheric end required to launch the wave.

[16] The free parameters in the model include the density $n(z)$ and composition $c(z)$ profiles, the equilibrium conductivities, Σ_{Po} and Σ_{Ho} (via P and H), the number of electron-ion pairs produced per incident electron, γ, the recombination coefficient, R, the ionospheric thickness through which the Pedersen currents flow, Δz, the perpendicular wave number, $k_\perp$, and the applied potential, $\Phi_o(t)$.

[17] The density and composition profiles have been determined largely by a statistical study of plasma densities from FAST observations between 21 and 03 MLT and over the altitude range from 400 to 4000 km. Figure 3 shows the profiles employed and is specifically for the polar cap boundary region near midnight but in daylight and without the effects of a potential drop. Consequently, in fitting the density profile to these points we have ignored those points in our database measured in ion beam regions. The diamonds on this plot represent the median density determined from the langmuir line, lower hybrid frequency, and whistler dispersion [*Strangeway et al.*, 1998] from 200 FAST orbits in 400 km bins starting from 400 km altitude. The error bars on each of these diamonds correspond to the range of densities observed in each altitude bin. At altitudes below the FAST spacecraft we rely on rocket measurements [*Knudsen et al.*, 1992] and radar measurements of densities in the ionosphere as reported by *Baron* [1974] and *Tsunoda* [1988]. At altitudes well above FAST apogee we have assumed densities representative of magnetospheric plasmas. The functional form of the density profiles used can be found in *Chaston et al.* [2002b].

[18] The applied potential is a Gaussian with an amplitude of 3600 eV and a full width at half maximum of 1s. This amplitude has been set so as to provide an $E_{\perp 1}$ of 300 mV/m at an altitude of 1700 km close to that observed in the case study discussed above. This value is dependent on the density and composition profile given in Figure 3 and provides a maximum wave amplitude of 1.5 V/m a few thousand kilometers above 1700 km. This is a very large electric field; however, such fields are observed occasionally by the FAST spacecraft at apogee [*Ergun et al.*, 1998]. Since it is our intent in this report to model the case study event described in section 2, which carries one of the largest Alfven wave Poynting fluxes observed from FAST, it is reasonable to consider a wave field model where such large amplitudes can occur.

[19] The perpendicular wavelength used is 5000 m at the ionosphere which according to the analysis of *Chaston et al.* [2002b] would provide an arc of the order of $\sim$1–2 km in width. The $k_\perp$ is then scaled in altitude with the square root of the geomagnetic field strength which is modeled as a dipole. The equilibrium height integrated Pedersen and Hall conductivities, $\Sigma_{Po,\,Ho}$ in the ionosphere are taken as 1 mho with $P = 3.0 \times 10^{-11}$ mho m^3 after *Lysak* [1991], and for simplicity we assume $P = H$. From the analysis of *Spiro et al.* [1982] this is appropriate for an average electron energy of 1 keV.

[20] Using these free parameters, equations (4) and (5) are solved using a leapfrog technique and a variable spatial step size in z determined by the inertial Alfven speed as a function of altitude and the time step to provide a Courant number of 1/2. The time step is set so as to provide a smooth waveform throughout and is 3 ms.

3.2. Ionospheric Feedback Interaction

[21] The source of free energy for wave growth inside the resonator is a localized reduction in Joule heating in the ionosphere [*Lysak and Song*, 2002] which enters the formalism used here through the convection electric field, $\mathbf{E}_o$. This field appears in equation (7) and through the convective flow, $\mathbf{v}_o$, in equations (8) and (9). For the sake of simplicity we choose $\mathbf{k}_\perp$ to lie at 90° to $\mathbf{E}_o$, which is appropriate for the polar cap boundary near midnight. Under these conditions the effects of gradients in the Hall conductivity are dominant. The magnitude of $\mathbf{E}_o$ at 100 km is taken to be 100 mV/m. This large convection electric field [*Ericksson et al.*, 2000] is selected since events such as the case study example here (where AE > 500) often occur during periods of large AE values and in association with geomagnetic substorms. Such a large value provides a strong ionospheric feedback interaction.

[22] To determine the number of electron ion pairs produced per incident electron, we rely on the results of *Rees* [1975] who shows that $\sim$46% of the incident electron energy goes into producing ionization of the major atmospheric species. Given that the ionization energy for components in the thermosphere range from 9.25 up to 15.6 eV per

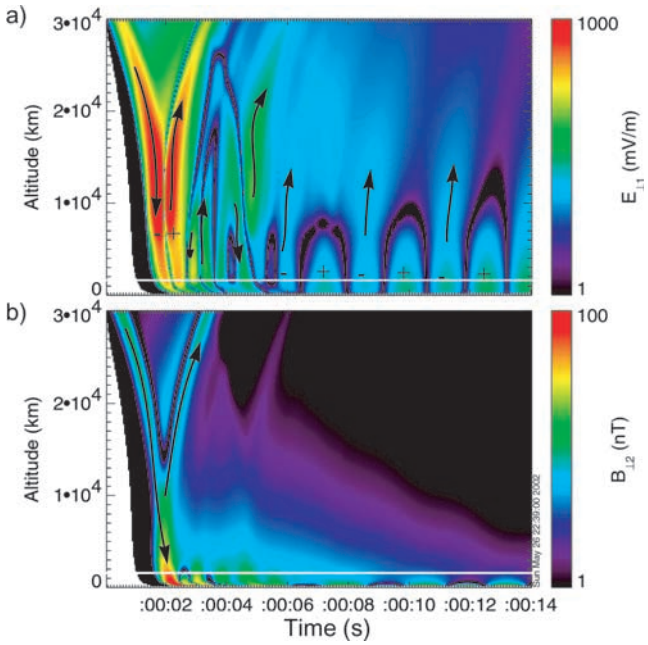

Figure 4. The Ionospheric Alfven Resonator. Electric (a) and magnetic (b) fields as functions of altitude and time from an applied potential at the high altitude (magnetospheric) end of the simulation. Arrows indicate direction of the wave group speed and the positive and negative signs indicate polarity. Here $\Sigma_{Po,Ho} = 1$, $\gamma = 1$ and $k_\perp$ in the ionosphere is $2\pi/(5000\ \text{m})$ and at 90° to E_o which is 0.1 V/m. The white line shows the FAST spacecraft altitude at the time of observation.

pair, for a 1 keV incident electron 30 ion-electron pairs may be produced or using the nomenclature from section 3, $\gamma = 30$. In the case of downward current in the Alfven wave or upward moving electrons, $\gamma = 1$. A value larger than this leads to an exaggerated feedback response where n_1 may rapidly exceed the equilibrium density, n_o, leading to negative densities in the boundary condition at 100 km. However, since we have Fourier transformed in the direction perpendicular to B_o it is only possible to specify one value for γ in this model. The 2-D case which relieves this restriction has been studied by *Lysak* [1986]. Instead, we examine the instability properties for $\gamma = 1$ here and $\gamma = 3$ in section 5.1. Both these values are sufficient to excite the feedback instability for the parameters used and provide amplitudes in the resonator up to 900 mV/m after a few cycles in the later case. Clearly, if such large amplitudes can be obtained for this value of γ, then the nonlinear response of the ionosphere becomes important in limiting wave amplitudes generated by this process to those observed.

[23] For the remaining parameters we rely on those given by *Lysak* [1991] with a recombination coefficient of $R = 3.0 \times 10^{-7}\ \text{cm}^3\ \text{s}^{-1}$ and an ionospheric thickness of $\Delta z = 50$ km.

[24] Figure 4 shows the wave fields of the ionospheric Alfven resonator unstable to the feedback instability from the simulation code in the $\gamma = 1$ case. The wave pulse can be seen entering the simulation from the top left in both Figures 4a and 4b and propagating down the field-line gradually increasing in strength in $E_{\perp 1}$ due to the convergence of the magnetic field and the increasing Alfven speed. The wave partially reflects off the Alfven speed gradient most strongly as its leading edge encounters the ionospheric density gradient above 5000 km. The reflected portion of the wave then travels upward and out of the simulation through the upper boundary at $t \sim 3.2$ s. A small fraction of this wave flux (~10%) is reflected back downward at the magnetospheric boundary to provide the enhanced electric fields seen at ~10000 km at $t \sim 5$ s in Figure 4a) and close to the magnetospheric boundary at $t \sim 6$ s in Figure 4b). The remaining portion of the initial downgoing wave continues to partially reflect as it travels downward yet reaches the ionosphere at $t = 2.3$ s where it is partially reflected upwards. This portion of the wave then travels back up the fieldline from the ionosphere but is partially reflected back down the fieldline by the Alfven speed density gradients that exist above the ionosphere as can be seen in Figure 4a at $t \sim 2.8$ s. The process of upward and downward reflection from the ionosphere and the gradients in the Alfven speed that exist above it continues as the wave is weakly trapped. This is the ionospheric Alfven resonator.

[25] The additional ionization caused by the incidence of the Alfven wave on the ionosphere eventually leads to the

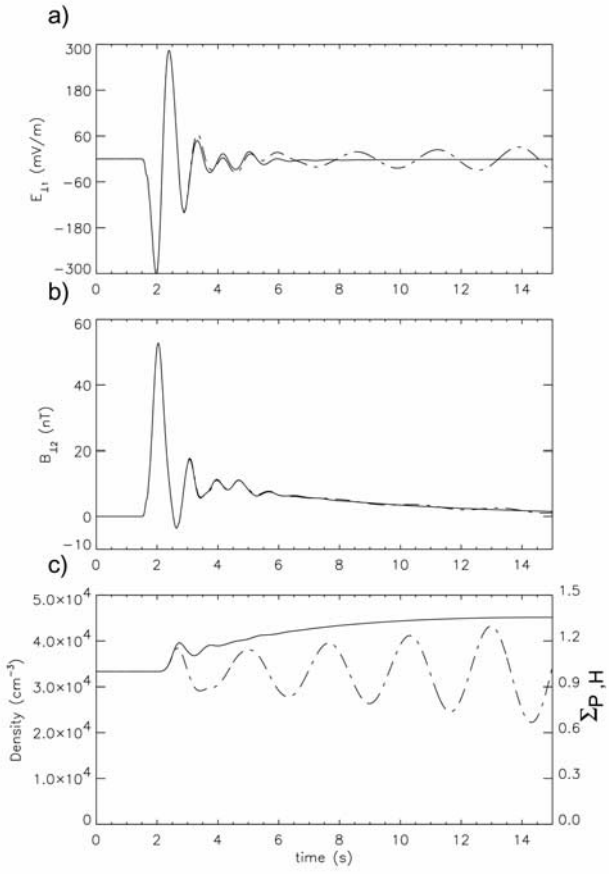

Figure 5. Wave field simulation results at an altitude of 1700 km for $\Sigma_{Po,Ho} = 1$ and $\gamma = 1$with $k_\perp$ at 90° to E_o. (a–c) Solid lines correspond to results with no convection electric field, $E_o = 0.0$, while dashed lines are those obtained from a slice through Figure 4 with $E_o = 100$ mV/m. Figure 5c shows the calculated density and conductivity variation in each case at 100 km altitude.

excitation of the ionospheric feedback instability seen here as the periodic structures at low altitudes which become visible after $t \sim 5$ s. The oscillations occur at a frequency of ~0.39 Hz which, as will be shown later for this case, is largely determined by the convection speed and the perpendicular wavelength of the wave in the ionosphere. Comparison of Figures 4a and 4b at these times reveals that the phasing between $E_{\perp 1}$ and $B_{\perp 2}$ is ~90° indicative of a standing wave. The upper boundary of the resonator is, however, not perfectly reflecting, and wave energy flux leaks out leading to waves with the same periodicity as the resonator traveling upwards into the magnetosphere from the top end of ionospheric density gradients shown in Figure 3.

[26] Figure 5 shows the wave fields from a slice through the simulation at 1700 km altitude as indicated by the white horizontal line through Figure 4. It is assumed for simplicity here and throughout the rest of this manuscript that the spacecraft is essentially stationary relative to the perpendicular wave phase speed. As a result all variation shown is temporal. Two cases are considered, one with the convection electric field turned off ($E_o = 0.0$, solid line) and one with the convection field turned on ($E_o = 100$ mV/m, dashed line). The initial pulse at 2.0 s in Figure 5a and 5b represents the downgoing wave from the magnetosphere after partial transmission through the strong Alfven speed gradient at altitudes above the ionosphere. The electric and magnetic field are π radians out of phase representing a downward going Poynting flux at this time. After reflection from the ionosphere, however, the phase difference approaches π/2 as the incident wave pulse bounces around inside the resonator cavity as described above. The wave fields in both the $E_o = 0.0$ and 0.1 mV/m cases remain essentially the same until t ~ 5 s. After this time in the convective case we see wave growth at a lower frequency. These oscillations are more clearly represented in $E_{\perp 1}$ than $B_{\perp 1}$ as the wave at this altitude is significantly more electrostatic than $E_{\perp 1}/B_{\perp 2} = V_A$ due to the operation of the resonator [*Lysak*, 1998]. The relative phase between the electric and magnetic field oscillations is ~π/2 representing a standing wave in the resonant cavity formed between the ionosphere and the Alfven speed gradient above it at ~0.39 Hz. The waveforms generated in this way with initially higher frequency oscillations excited by the incidence of the initial pulse on the resonator and then, in the convecting case, lower frequency resonant fluctuations, as shown in Figure 5a, is similar to the observed wave fields shown in Figure 1b.

[27] Figure 5c shows the density and conductivity variations at 100 km altitude in the ionosphere due to this interaction. The enhancement in density at $t = 2.75$ s is delayed relative to appearance of the wave at 1700 km owing to the propagation time. In the nonconvecting case (solid line) the conductivity/density after the initial increase associated with the arrival of the wave at the ionosphere decreases slightly due to recombination and the reversal of the field-aligned current direction. However, after $t \sim 3$ s, the current while oscillating remains directed upwards (indicated by the positive $B_{\perp 1}$, with from earlier $j_z = (k_\perp^2 A_z)/\mu o$ and $B_{\perp 2}(x,z,t) = \cos(k_\perp x) \cdot k_\perp(z) Az(z,t)$) thereby providing a continuous source of ionization leading to the monotonic density and conductivity increase obtained after this time. This enhancement will be spatially periodic, with an equal yet opposite change in conductivity/density at $x = 2\pi/k_\perp$. In the convecting case the spatial periodicity in j_z leads to an oscillatory variation in Σ_1 and n_1. This oscillation has a frequency given by $\mathbf{E_o} \times \mathbf{B_o}/(B_o^2 \cdot (\lambda_\perp = 5000$ m)) = 0.39 Hz and drives the resonator at this frequency to provide the oscillations seen in the fields quantities in Figures 5a and 5b.

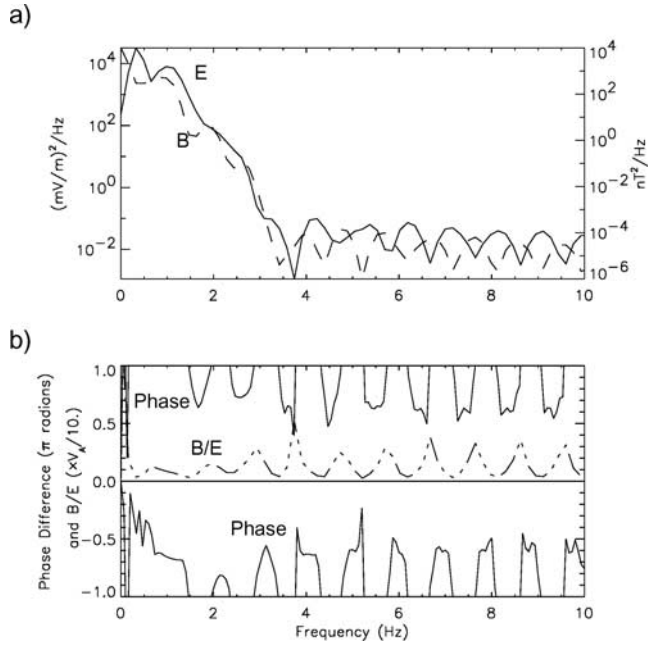

Figure 6. Spectral structure of the simulated wave fields shown in Figure 4 and 5 with $\Sigma_{Po,\ Ho} = 1$, $\gamma = 1$ and $k_\perp$ at 90° to E_o inside the resonator at an altitude of 1700 km. (a) The wave power spectra from $E_{\perp 1}$ (solid line) and $B_{\perp 2}$ (dashed line). (b) The phase of $E_{\perp 1}$ relative to $B_{\perp 1}$ (solid line) and the value of the ratio $B_{\perp 1}/E_{\perp 1}$ (dashed line) times $V_A/10$. The wave coherency is above 0.8 throughout.

[28] Figure 6 shows the spectral features of the case with the convection field turned on. The electric (solid line) and magnetic (dashed line) fields spectra shown in Figure 5a have peaks at a frequency of 0.39 Hz (f_f) and then smaller enhancements at ~0.8 Hz intervals. In this sense the oscillator obeys $f_h = f_f x(1, 3, 5, \ldots)$ representing an odd resonance with a node at the ionospheric end and an antinode at the top end of the resonator and the reverse for the magnetic field. This is the case where $\Sigma_p > \Sigma_A$ in the ionosphere where qualitatively the Alfven wave sees the ionosphere as a conductor. The spectra in this case result from the position of the observation point relative to the location of the nodes and antinodes occurring over the length of the resonator for a given wave frequency. The spectral peaks in $E_{\perp 1}$ and $B_{\perp 2}$ are almost anticorrelated as expected for a standing wave where the relative phase between $E_{\perp 1}$ and $B_{\perp 2}$ approaches +/− π/2. This phase relationship can be seen in the $E_{\perp 1}$ and $B_{\perp 2}$ cross-spectral phase results shown in Figure 5b. The basic phase structure is that expected for the resonator with phase approaching +/− π/2 (solid line). There are in addition peaks in the ratio of $B_{\perp 2}/E_{\perp 1}$ (dashed line in Figure 5b) at frequencies where a node in $E_{\perp 1}$ occurs

at the altitude of observation (and where antinode occurs in $B_{\perp 2}$).

4. Electron Acceleration

4.1. Electron Model

[29] By using the wave model established above we can determine the form of the observed electron distributions as a function of altitude and time through the use of test particles distributed along the fieldline representing the various electron components present. Since the electron number density varies by more than five orders of magnitude along the fieldline it is not possible to replicate the density distribution on which the wave model is based and complete the simulation in reasonable times. Instead, we employ a maximum of 20,000 electrons in the modeling and distribute them along the field line in a way dependent on the component which they represent as will be described. These electrons are accelerated in the simulated Alfven wave field according to the Lorentz force and the trajectory of each determined using a fourth-order Runge-Kutta technique.

[30] We use a two-electron component plasma representing the ionospheric electron and photoelectrons in the polar wind which have convected into the poleward edge of the auroral oval. We have not included the plasma sheet electrons in this simulation as the accelerated portion of the observed distribution is comprised primarily of cool electrons. Since the observed event occurred in daylight, the scale height of the ionosphere is significantly larger than for the usual dark auroral ionosphere used in models of this type. With this in mind we distribute these electrons as a Maxwellian with a temperature of 2 eV with decreasing den-sity up to 10000 km altitude. The polar wind photoelectron component here is modeled as a 30 eV Maxwellian distri-buted evenly along the fieldline from the ionosphere to 24000 km. Once the simulation has begun, the ionospheric and polar wind electrons are introduced at random heights (weighted by their altitude distribution) from the sides to maintain roughly the same number of active electrons throughout the simulation. The physical basis for the seeding of the flux tube in this way is not well established; however, convection of cool plasma from the polar cap into the poleward boundary of the auroral oval is consistent with this approach and much of the ionospheric and photoelectrons lost through precipitation are in fact reintroduced naturally at higher altitudes as the wave accelerates electrons back up the fieldline.

4.2. Single Particle Results

[31] Figure 7a shows the parallel electric field profile, $E_{\|}$, from the simulation with E_o = 0.1 mV/m. Since the parallel electric field is related to the applied potential through a spatial derivative along the field-aligned direction, the wave appears as a bipolar pulse indicated by the positive and negative signs on the incoming and outgoing wave fields. As the wave encounters the ionospheric density gradient, its leading edge travels more slowly than the rest of the waveform, and the wave field tends to "pile up" over a region spanning ~4000 km in altitude causing the hump in parallel field amplitude at 8000 km shown clearly by the solid line in Figure 7b and providing parallel electric fields exceeding 0.1 mV/m down to 4000 km altitude. At this time the amplitude of the parallel field is almost twice that predicted by equation

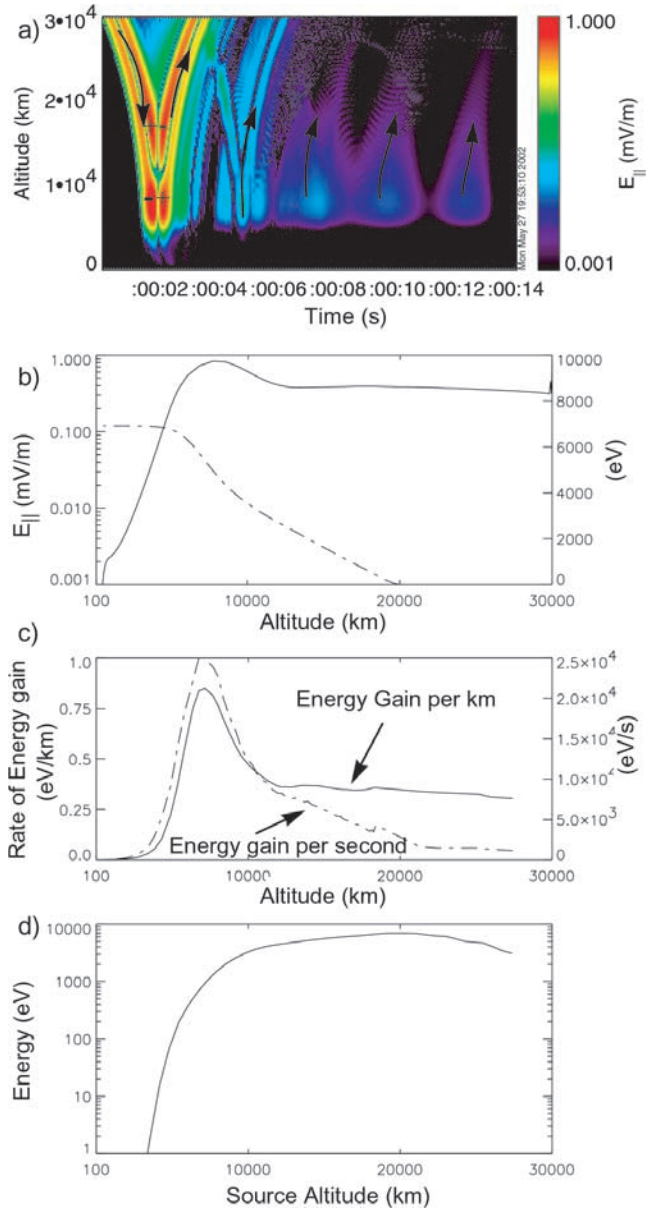

Figure 7. Electron acceleration. (a) The parallel wave electric field, $E_{\|}$, as a function of altitude and time. Arrows show the direction of the wave group speed with negative sign indicating an upward pointing electric field and positive sign indicating a downward pointing electric field. (b) The solid line shows the amplitude of the wave electric field in the initial downgoing pulse (i.e., bright red curve with increasing slope in Figure 7a) while the dot-dashed curve is the energy of an electron accelerated by this pulse from an altitude of 20000 km. (c) The rate of energy gain for a single electron in eV/km (solid line) and eV/s (dot-dashed line). (d) The dependence of energy gain on the source altitude of the electron in the downgoing wave.

(3) from the local approximation. This provides for a short time a standing wave with a parallel potential drop of a few keV before the wave reflects and travels back up the fieldline. Not surprisingly, Figure 7c shows that it is at this altitude (and this phase of the simulation) that the electrons experience the greatest rate of energy gain. Steeper density gradients at

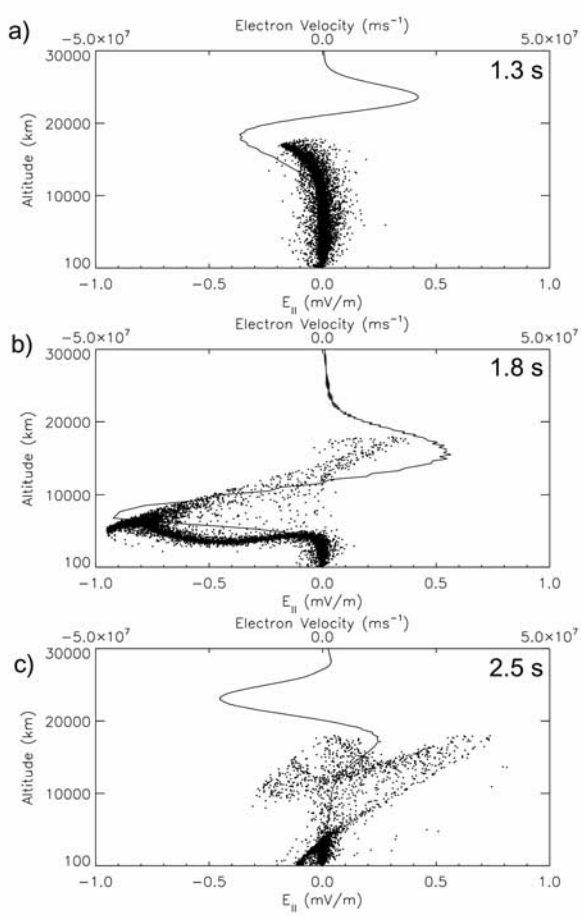

Figure 8. Snapshots of the simulation. The solid line is the parallel electric wave field while the dots represent electrons. Positive velocities are upward and negative are downward. (a) The wave shortly after entering the box. (b) The wave in the process of reflection and (c) the wave propagating back up the fieldline.

lower altitudes (for instance that existing at the base of a field-aligned potential drop [*Ergun et al.*, 2000]) enhance this effect to allow electron acceleration to slightly greater energies than for the sunlit electron density profile used here [*Chaston et al.*, 2002b].

[32] The actual total energy gain for an electron is dependent upon the phase at which it encounters the wave and the altitude from which the particle becomes resonant. For the density and composition profile used here, Figure 7d shows that the most energetic electrons for the parameters of this model will become resonant with the wave from ~20000 km and reach an energy of ~7 keV. Electrons picked up by the wave at lower altitudes (and higher) gain progressively less energy since they are not phased correctly to experience the greatest kick from the parallel wave field as it reflects.

[33] At altitudes below ~4000 km or within the resonator region the energy gain for electrons is small. Figures 7a and 7b show that the magnitude of the wave parallel field below the peak falls quickly as the density increases and the skin-depth becomes rapidly much less than the perpendicular wavelength. This result is represented in the unchanged electron energy shown by the dashed-dotted line at altitudes below 4000 km in Figure 7b, the decline in the rate of energy gain for an electron in the downgoing incident wave shown in Figure 7c below 8000 km, and the result that an electron from a source altitude of less than 3000 km will gain less than 10 eV in the wave field shown in Figure 7d. Furthermore, Figure 7a shows that the weakly unstable feedback interaction in this case generates negligible parallel fields at resonator altitudes and does not provide fields exceeding 0.001 mV/m until part of the wave field has leaked through the top end of the resonator above ~5000 km where densities are sufficiently small for a significant electron inertial effect.

4.3. Multiple Particle Results

[34] Figure 8 shows three snapshots taken from the simulation based on the wave field with E_o = 0.1 mV/m. The wave is a bipolar pulse shown by the solid trace in the center of Figures 8a, 8b, and 8c. The dots represent ionospheric and polar cap electrons distributed along the field line as discussed in section 4.1. The ionospheric electrons are the closely spaced dots close to zero velocity while the polar cap electrons are the less densely spaced dots at larger velocities.

[35] Figure 8a shows electrons being accelerated in the wave field at altitudes above 15000 km. The left side (negative) of this plot shows electrons moving down the fieldline while the right side (positive) shows upward moving electrons. Electrons are accelerated downward in the upward pointing parallel electric field in the wave front as the wave travels down the fieldline. The magnitude of the field over this altitude range is shown in Figure 8a (solid line) and is such that the potential in the wave front is significantly larger than the energy associated with the wave phase speed. Consequently, most of the ionospheric and polar wind electrons are accelerated up to the wave phase speed over distances less than $\lambda_{||}/2$. This can be demonstrated from Figure 7c which shows that at these altitudes an electron gains ~0.8 eV/km and so is accelerated up to the wave phase speed of ~10^4 km/s over a distance of a few 100 km. This means that most of the cool electrons encountered by the wave are accelerated down the field line resulting in a depletion of the cold plasma density on the flux tube. As an aside, this may be a simple explanation for the observation of density cavities al lower altitudes as observed from the Freja [*Stasiewicz et al.*, 1997] and FAST [*Chaston et al.*, 2000b] spacecraft.

[36] Figure 8b shows the wave just before strong reflection on the steep Alfven speed gradient where ionospheric densities become dominant. The enhanced wave field amplitude and the "pile-up" mentioned in section 4.1 that occurs here are apparent as the waveform appears compressed on the low altitude end. At higher altitudes the opposite polarity portion of the wave field can be seen to accelerate electrons back up the fieldline. Figure 8c shows the waveform after reflection and shows counterstreaming electron acceleration. This portion of the simulation corresponds to the red streaks show in Figure 7a with positive slope. The wave phase has reversed, and at low altitudes we see a downward pointing electric field with an upward pointing field at higher altitudes. The electron acceleration

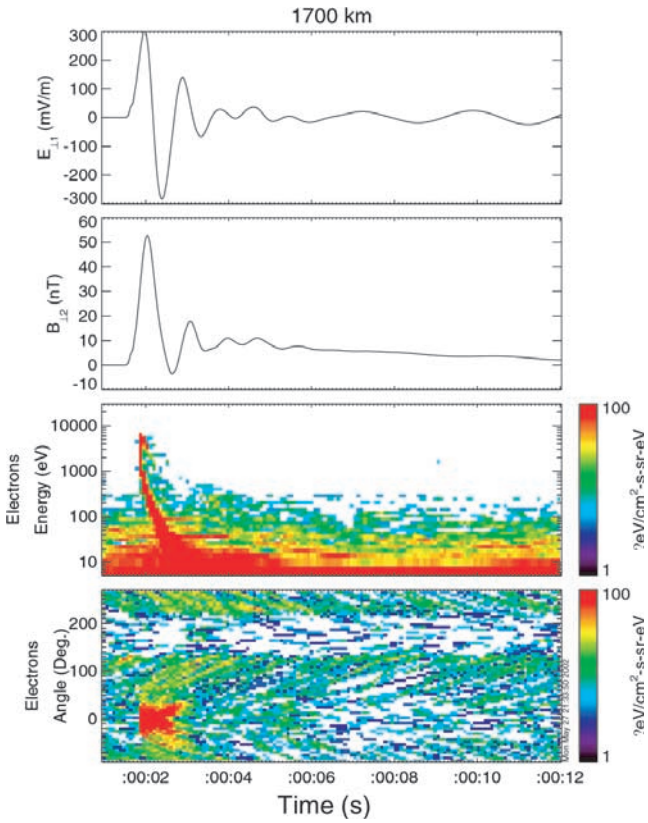

Figure 9. Simulated FAST measurements at 1700 km altitude with $\Sigma_{Po,\,Ho} = 1$ mho, $\gamma = 1$, and $E_0 = 0.1$ V/m and $k_\perp$ at 90° to E_o. The first and second panels show the simulated wave fields $E_{\perp 1}$ and $B_{\perp 2}$. The third and fourth panels are the simulated electron energy and pitch angle spectra.

that this wave field causes in the upward direction (right side of Figure 8c) is a resonant process similar to that for the incident downgoing pulse but instead the wave phase speed decreases in time. Consequently, the maximum energy attained is somewhat less than in the downgoing wave. Nonetheless, these electrons will be accelerated outwards and hence provide a source of cold ionospheric electrons distributed as field-aligned beams in the magnetotail.

[37] The electron acceleration in the downward direction (left side of Figure 8c) at this time is a nonresonant interaction since the wave field and the electrons move in opposite directions. Effectively, these electrons see a potential drop moving up the fieldline through which they fall. (In fact the downgoing wave also accelerates electrons up the fieldline in this way.) Consequently, a spacecraft passing through altitudes above 3000 km at this time will see counterstreaming electrons as previously shown by *Chaston et al.* [2002a].

[38] In all three snapshots the electrons from altitudes below ~4000 km remain largely undisturbed indicating very little electron acceleration at these heights and within the ionospheric Alfven resonator. The limited electron acceleration that occurs within the resonator region is due to some extent on the reflection of much of the incident magnetospheric wave Poynting flux on the steep gradients in the Alfven speed that exist above this altitude so that only a fraction of the wave energy is transmitted into the resonator below. However, it will be demonstrated later in section 5.1 that for realistic field amplitudes within the resonator region, greater than 100 eV electron acceleration in this region and in the linear approximation is unlikely.

4.4. Spectral Results

[39] By including a large number of electrons in the simulation as described in section 4.1 we can directly compare the observed electron energy spectra and distributions with the simulation results. Figure 9 shows results observed from a virtual FAST spacecraft immersed in the simulation at an altitude of 1700 km under the assumption that what FAST observed in the case study event was mainly temporal. The first two panels show the simulated perpendicular electric field and magnetic field as discussed in section 3. These time series are qualitatively similar to those shown in Figure 1b, however the amplitude of the magnetic field in the incident pulse is less than observed by a factor of 2 providing an $E_{\perp 1}/B_{\perp 2}$ ratio larger, by the same factor, than observed. For the traveling Alfven wave this results from the different density and composition at this altitude in the statistical model from that observed in the case study example.

[40] The simulated electron spectra at 1700 km altitude is shown in the third and fourth panels of Figure 9. As in Figure 1, −90 to 90 degrees pitch angle correspond to downgoing electrons while 90 to 270 degrees correspond to upgoing electrons. The incident wave here can be seen to provide two dispersive bursts of electrons. The first and most energetic starting at $\sim t$ = 2 s is due to electrons accelerated downward in resonance with the downgoing pulse as shown in Figures 8a and 8b of section 4.2. The electrons arrive on the leading edge of the initial pulse in $E_{\perp 1}$ and $B_{\perp 2}$ in a manner similar to that observed. The electron time dispersion results from the fact that there is little electron acceleration below 3000 km altitude in this model. This occurs in the way described by *Kletzing and Hu* [2001]. Calculation of the source altitude from this dispersion in the usual way yields ~5000 km which is the altitude where (with reference to Figure 7b) the wave parallel electric field starts to rapidly decrease. The pitch angle spectra given in the bottom panel shows that this burst of electrons is strongly field-aligned and falls well within the electron source cone (i.e., the range of pitch angles containing electrons which are lost to the ionosphere). The second burst of electrons beginning at t = 3.5 s has significantly lower energies and fluxes (barely visible in the spectral plot) than the first and arises from electron acceleration in the upward pointing parallel electric wave field in the reflected wave. The fluxes in this burst are insufficient to appear as a distinct feature in the pitch angle plot in part due to the depletion of electron density along the flux tube associated with the "snow plow" like effect of the first field pulse. This burst corresponds to the downgoing electrons shown in the snapshot at 10000 km in Figure 8c and discussed in section 4.3. Since these electrons are accelerated at higher altitudes than the first dispersive burst they have extended dispersion times. Subsequent to this burst there is very little electron acceleration in this model. The parallel field in the resonator that remains is too small to accelerate the electrons to more than a few tens of

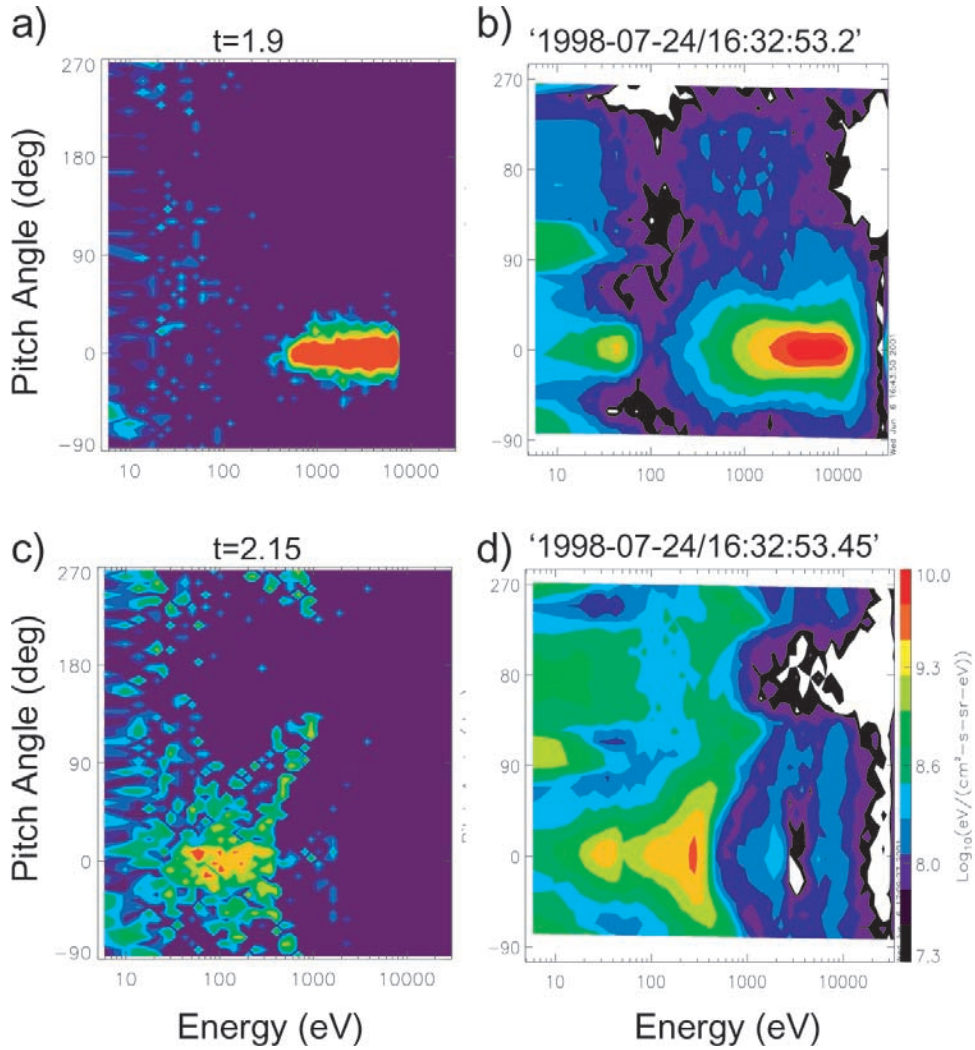

Figure 10. Comparison between simulated (a and c) and observed (b and d) electron pitch angle/energy distributions at two different times from the first dispersive electron burst shown in Figure 1b and Figure 9.

eV. These low energy electrons are represented in Figure 9 by the enhanced fluxes extending from $t = 2.5$ to $t = 7$ s at energies below 30 eV.

[41] Figure 10 shows two snapshots of the observed and simulated electron distributions during the dispersive electron burst at 16:32:53.5 shown in Figure 1b and 1.8 s in Figure 9. In Figures 10a and 10b the highest energy portion of the simulated and observed burst is displayed showing accelerated polar cap electrons and ionospheric electrons up to energies of 7 keV in the simulation and exceeding 10 keV in the observations. Figures 10c and 10d show snapshots taken 0.25 s apart through the dispersive burst in each case. The forms of the simulated and observed distributions in pitch angle/energy space are very similar. The higher energy bowl like peak in the downgoing electron distribution is due to the significant perpendicular energy of the accelerated electrons many of which mirror at this altitude leading to enhanced fluxes at 90 and 270 degrees and electron conics [*Andre and Eliasson*, 1992]. These electrons have received more energy from the wave than the lower energy more field-aligned electron peak shown in this snapshot. This is because they have a higher source altitude but however take longer to arrive at the spacecraft than the more field-aligned electrons from the same source altitude due to deceleration by the mirror force. This component is composed of polar cap electrons while the lower energy field-aligned electron peak seen here is composed of ionospheric electrons accelerated at altitudes only a few thousand kilometers above the spacecraft.

[42] While the observed and simulated electron distributions and time series electric and magnetic fields are similar, the observed time variant electron spectra shown in Figure 1b shows considerably more structure than seen in the simulation with several more field-aligned electron bursts at energies less than 100 eV. Assuming that the energy-time dispersion provides a reasonable estimate of the source altitude, the electron acceleration in the first burst, starting at 1632:53.5 UT, appears to be occurring at altitudes of the order of ~5000 km or approximately the same altitude as simulated. The next two dispersive bursts at 1632:54 and 1632:55 UT have somewhat higher source altitudes and lower energies comparable with the simulation result for the second field-aligned burst. Subsequent lower energy bursts observed are not reproduced at all in the simulation.

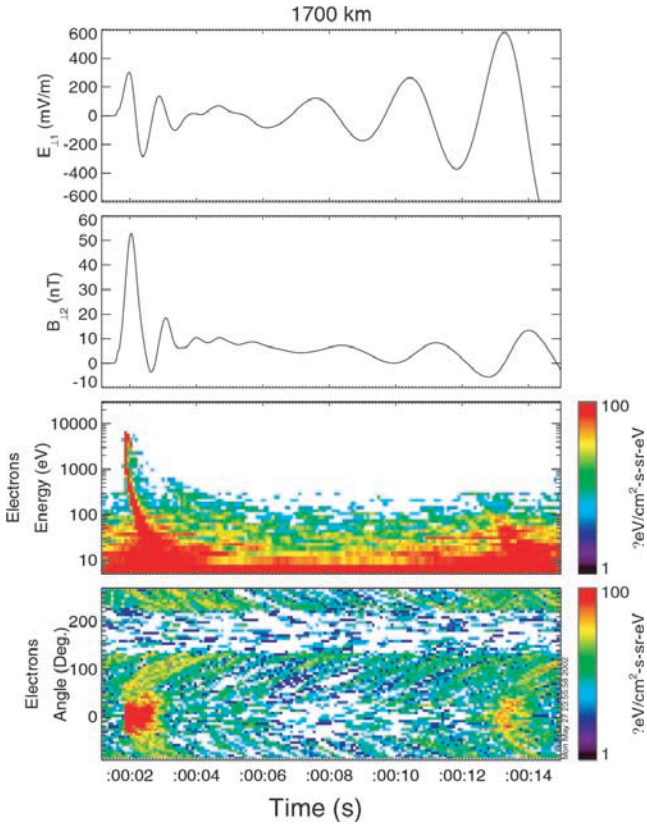

Figure 11. Simulated FAST measurements at 1700 km altitude with $\Sigma_{Po,\ Ho}$ = 1 mho, γ = 3, and Eo = 0.1 V/m and $k_\perp$ at 90° to E_o. The first and second panels show the simulated wave fields $E_{\perp 1}$ and $B_{\perp 2}$. The third and fourth panels are the simulated electron energy and pitch angle spectra.

We will now discuss how the additional lower energy bursts may arise.

5. Discussion

[43] Many of the observed features of electron acceleration and Alfvenic waveforms observed in the high-latitude auroral oval can be qualitatively explained through the Alfven wave acceleration of electrons at altitudes above the ionospheric Alfven resonator and by the oscillatory fields created by the resonators operation. These include dispersive electron bursts, field-aligned electron distributions, electron conics, wave spectra peaked at ~0.1–1 Hz, and for this case study temporally decaying oscillatory wave fields.

[44] There are however significant differences between the simulation results and observations. If we are to assume that the accelerated electrons observed after the first field deviation and dispersive electron burst in Figure 1b are due to acceleration in the resonating wave field then it would appear that the observed resonating Alfven wave in this case study can continue to accelerate electrons to energies greater than of 100 eV at much smaller wave amplitudes within the resonator region than found in the simulation. Furthermore, the peak energies reached of ~7 keV are several keV less than the peak energy observed, which from Figure 1b exceeds 10 keV. Lower mass densities along the field line may allow electron acceleration to greater energies owing to the larger phase speeds and a stronger electron inertial effect than employed here for the sunlit case. This will be true for density and composition profiles above the auroral ionosphere in darkness and as mentioned in section 4.2 particularly in the presence of a quasi-static field-aligned potential drop. Other than this possibility, and if we accept for the moment that the observed electron acceleration is purely due to the electron inertial effect, then there are several possible shortcomings in the simulation that may allow the Alfven wave to provide greater energies at low altitudes. The first of these is the model ionosphere which we now make significantly more unstable to the feedback instability.

5.1. Electron Acceleration in a Strongly Unstable Ionospheric Alfven Resonator

[45] *Lysak* [1991] has shown how changes in ionospheric conductivity due to electron precipitation can excite a feedback instability allowing wave growth within the resonator to nonlinear levels. These large amplitude waves may then accelerate electrons. To examine the ability of these wave fields to accelerate electrons in the resonator region we have performed the same test particle simulation as presented in section 4 using a wave model strongly unstable to the feedback instability with γ = 3. As indicated in section 3.1, this value is incorrect in the downward current region, yet we use it here to pump large amplitude waves from the ionospheric boundary into the resonator to examine the ability of these waves in this region to accelerate electrons.

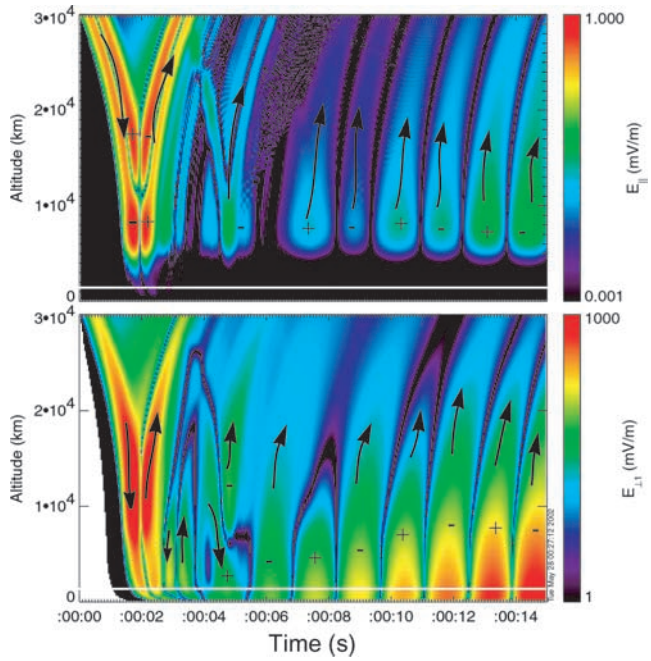

Figure 12. Strongly unstable Alfven resonator. Here $\Sigma_{Po,\ Ho}$ = 1.0, γ = 3, E_o = 0.1V/m, and $k_\perp$ is at 90° to E_o. Arrows show the direction of the wave group speed while positive and negative signs show polarity. The white line shows the altitude of the FAST spacecraft.

[46] The results from this simulation are shown in Figure 11 where it can be seen that while the simulated wave fields are considerably different from those shown in Figure 9 (and from those observed in Figure 1b) the simulated electron energy spectra remains not greatly changed from the case without the feedback instability in operation. The growing wave fields do eventually make a difference as can be seen at the far right side of electron spectral results with the appearance of dispersive field-aligned electron bursts at energies below 100 eV. However, this result requires very large amplitudes in the resonator which are in fact significantly larger than that which is observed. The explanation for the inability of these waves (except with very large amplitudes) to provide significant electron acceleration is that for observed plasma densities and perpendicular scales within the resonator region it is difficult to generate an appreciable parallel field.

[47] This fact is demonstrated in Figure 12a where we plot the amplitude of the upward pointing parallel field. In Figure 12b we plot the perpendicular electric field for the same case. This figure shows that while the perpendicular wave field driven by the feedback instability peaks at ~600 km with an amplitude of over 900 mV/m, Figure 12b shows the parallel field that results from this interaction at this altitude is less than 0.01 mV/m. This is because the wave at this altitude is only weakly inertial. The small $E_{\parallel}$ that results provides almost no electron acceleration.

[48] The parallel field however does increase rapidly in altitude once outside the region dominated by ionospheric plasmas toward a peak at 8000 km yet remains less than 0.1 mV/m throughout. This peak occurs outside the resonator region where the wave field appears as oscillations traveling up the fieldline "leaking" from the top of resonator. It is $E_{\parallel}$ at this altitude, generated remotely by the feedback instability of the ionospheric Alfven resonator operating below that eventually provides the low energy dispersive electron bursts observed in the far right of Figure 11.

[49] Despite the large $E_{\perp}$ generated by the feedback instability at the lower altitudes where the resonator is operating, it is difficult to obtain larger parallel fields at altitudes where the inertial effect is significant (and hence larger electron energies) for realistic perpendicular field amplitudes inside the resonator. This is because the wave energy generated by the feedback effect is largely reflected at altitudes well below where significant parallel fields are possible. This can be seen in Figure 12a where the magnitude of the perpendicular electric wave field decreases with increasing altitude above the ionosphere despite the increasing Alfven speed (or E/B ratio) over this altitude range (as shown in Figure 3).

[50] The results presented in Figure 11 and 12 are specific for the density and composition profiles and wave number employed. Varying these profiles within observable limits alters the specific results, however for the alternate parameters tested this does not appreciably alter the strength of the parallel field within the resonator. One solution to the problem of creating parallel electric fields is by making the "top end" of the resonator more transparent to the up coming (and downcoming oscillations) to increase the wave energy at altitudes where $E_{\parallel}$ is more easily supported. This however, tends to stabilize the feedback instability. Alternatively, electron acceleration over a wider range of altitudes and well within the resonator may be possible with the inclusion of a spectra of perpendicular wave numbers. This can be understood from equation (3) since larger $k_{\perp}$ allows the wave field to carry a significant $E_{\parallel}$ to lower altitudes (i.e., where the densities are higher and λ_e is smaller). The improvements of this addition are however limited since from equation (1) the wave phase speed decreases with $k_{\perp}^2$. Consequently, while the parallel field at higher plasma densities may be increased with a larger $k_{\perp}$, the amount of energy gain through resonance with wave is reduced. We have in fact performed the simulation for a range of wave numbers and have found that from $k_{\perp} = 2\pi/2$ to $2\pi/10$ km there is little variation in accelerated electron energy but that this energy falls quickly outside this range [*Chaston et al.*, 2002b]. Finally, Alfven waves particularly at lower altitudes are often observed to be propagating in density cavities which may also allow the wave to carry a larger parallel field component than predicted in the model used here. However, for the case study considered the density fluctuation is less than 1% and so provides only an insignificant correction to $E_{\parallel}$ and hence also an insignificant change to the electron energies obtained.

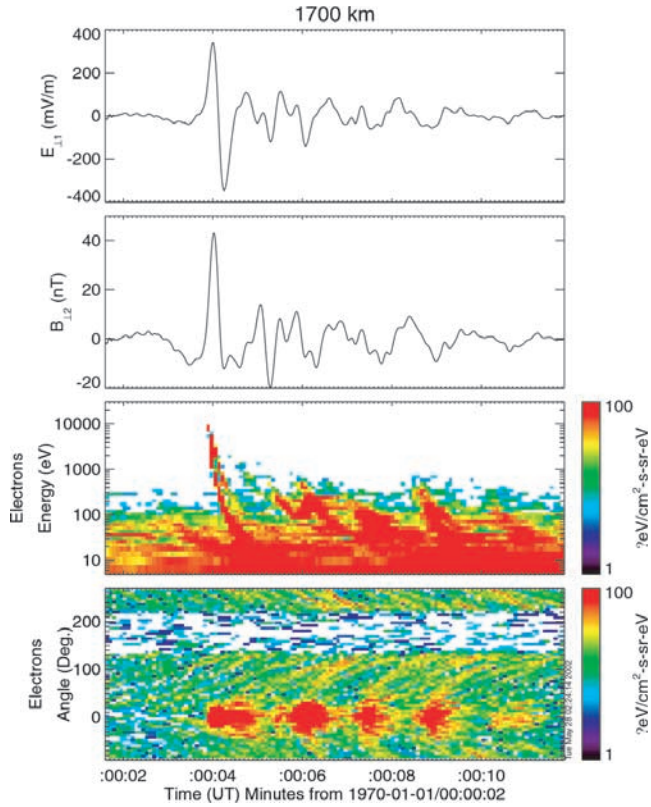

Figure 13. Simulated FAST measurements at 1700 km altitude for a data based wave potential applied at the top of the simulation box. Here $\Sigma_{Po,\,Ho} = 1$ and $E_o = 0.0$ V/m. The first and second panels show the simulated wave fields $E_{\perp 1}$ and $B_{\perp 2}$. The third and fourth panels are the simulated electron energy and pitch angle spectra.

[51] This suggests that if indeed we are observing electron acceleration due to the reflecting wave in the resonator then this wave is capable of producing a larger parallel electric field than found from electron inertial effects in a

linear model. 3-D electric field observations [*Chust et al.*, 1998; *Chaston et al.*, 1999; *Ergun et al.*, 2001] suggest that the wave may be capable of producing a very large parallel field at resonator altitudes but the means by which this occurs is not understood.

5.2. Driven Oscillations

[52] An alternative explanation to the feedback interaction is that the observed electron acceleration is continuously driven from a source outside the resonator [*Chaston et al.*, 2002a]. This still retains the spectral structure of the resonator to account for phase observations shown in Figure 2 while allowing the wave field access to that altitude region just above the resonator region where the inertial effect and electron acceleration are greatest. Figure 13 shows the electron spectra and wave time series at 1700 km altitude that results from applying a potential at the top of the simulation box derived from the magnetic field measurement shown in Figure 1b but scaled as previously to provide a maximum amplitude of 1.5 V/m at some altitude. The resulting time series electric and magnetic field measurements at 1700 km not surprisingly show considerably more structure than found for the Gaussian potential. The effect of reflection inside the resonator also alters the incident waveform from that shown in Figure 1b but nonetheless similarities remain. The electron spectra contains multiple dispersive bursts with decreasing peak energy for each successive burst similar to the observations shown in Figure 1b. The peak energy of the first of these is 1 keV higher than found for the Gaussian pulse of the same amplitude shown in Figure 9. This results because of the initial upwards acceleration provided by the slight rise in the electric field strength (Figure 13, first panel, $t \sim 3$ s) that precedes the arrival of the pulse at all altitudes. These upgoing electrons are then reflected in the wave front of the downgoing wave to yield slightly higher energies.

[53] While the structure of this simulated result is similar to that observed the simulated wave is significantly more electrostatic than observed. This is largely due to the statistically derived density and composition profiles, however for density and composition profiles within the range of observations and wave amplitudes less than 1.5 V/m at all altitudes it seems not possible to reproduce the observed amplitudes, $E_{\perp 1}/B_{\perp 2}$ ratio and multiple keV electron acceleration simultaneously in the same model. This is because increasing the oxygen density at the altitude of observation, for consistency with the observed $E_{\perp 1}/B_{\perp 2}$ ratio (in the initial field spike where the wave is traveling), significantly reduces the wave energy flux that penetrates in the traveling wave to this altitude. With this in mind even in the driven case there appears to be additional effects not considered that allows the incident wave (or pulse in this case) to experience less reflection from the Alfven speed gradient on the topside of the Alfven speed peak. This is necessary to account for observed wave amplitude of the incident pulse at 1700 km before reflection from the active ionosphere while still retaining realistic wave amplitudes everywhere else.

5.3. Energy Dissipation

[54] The ability of Alfven waves with $k_\perp \lambda_e \leq 1$ to efficiently accelerate electrons means that they are subject to strong damping [*Lysak and Lotko*, 1996]. Consequently, the results of the test particle simulations performed are only meaningful if the Alfven wave is sufficiently energetic to account for the electron energy fluxes produced. To address this issue we have calculated the wave Poynting flux and estimated the electron energy flux from the driven simulation discussed in section 5.2 as functions of altitude and time. The results are shown in Figure 14. Positive slopes here indicate upward traveling fluxes while negative slopes indicate downward traveling fluxes.

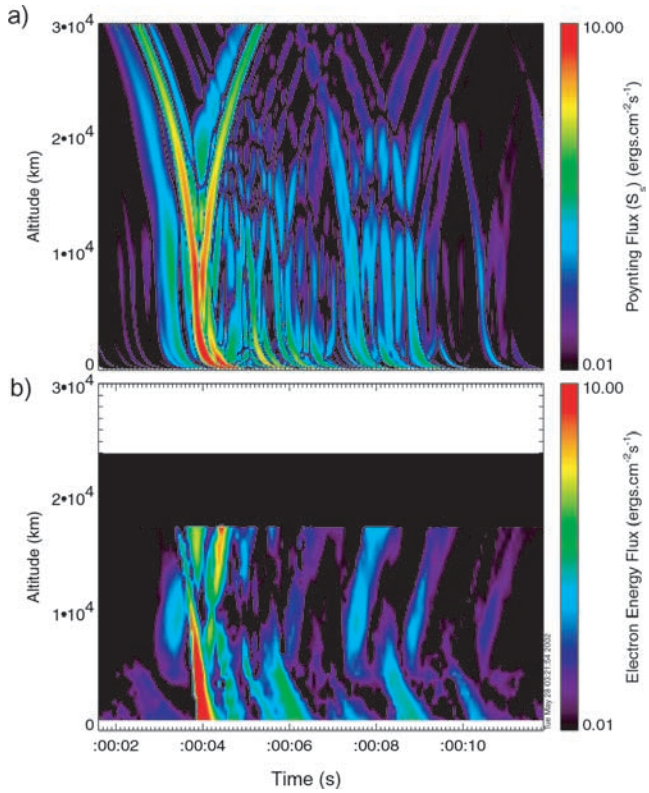

Figure 14. Simulated field-aligned wave Poynting flux (a) and electron energy flux (b) as functions of altitude and time. Upwards fluxes are patches with positive slopes in altitude with time while downgoing fluxes have negative slopes. The cutoff in the electron energy flux shown in Figure 14b at 18,000 km represents the maximum altitude to which the electrons are traced in the simulation.

[55] From the wave Poynting flux result, shown in Figure 14a, the incident wave pulse can be seen to propagate down the field-line gradually increasing in strength with the convergence of the magnetic field. The wave strongly reflects below 10000 km before reaching to the ionosphere with approximately half of the incident wave Poynting flux reflected back up the field line between this altitude and 5000 km altitude. Further fluctuations in the applied potential at the magnetospheric end can be seen to travel down the field-line at later times. At the base of the simulation in the ionosphere the wave has maximum Poynting flux of 15.3 erg cm^{-2} s^{-1}. The reflected upgoing wave Poynting flux at this boundary is significantly less than the incident wave Poynting flux as much of the wave energy is absorbed here for $\Sigma_{po} = 1$ [*Lessard and Knudsen*, 2001]. Increasing

the conductivity of this boundary increases the magnitude of the reflected wave Poynting flux.

[56] The energy flux scale presented in Figure 14b has been estimated by averaging the value of $1/2\ mv^3$ from each particle in altitude bins of 400 km and then multiplying by the density from Figure 3 at the center altitude. Since we do not trace the electrons above an altitude of 18,000 km, the energy fluxes are artificially terminated here. At altitudes below 4000 km the downcoming electrons are largely free-streaming since, as shown in Figure 7d, there is almost no acceleration here. Also in this region the density represented by the number of electrons in the simulation is the most inaccurate. Consequently, since the wave picks up very few new particles in this region, the density used in the estimation of wave enhanced electron energy flux below 4000 km is given by the density at 4000 km corrected for the converging magnetic field.

[57] The electron energy flux, shown in Figure 14b, looks similar to the wave Poynting flux over the first 5 s with electrons accelerated down the field line with the downgoing wave and up the fieldline in the reflected portion of the wave. The maximum electron energy flux at the ionosphere due to the acceleration process is estimated as $\sim$76 ergs $cm^{-2}\ s^{-1}$. At later times (4.5, 6.0, 7.5, 9, and 10.3 s) there a number of bursts of downgoing field-aligned electrons with smaller energy fluxes and considerably less structure than found in the simulated Poynting flux. Above 5000 km (and above resonator altitudes) at $t = \sim$4, 6.25, 9, 10.5 s and altitudes above there are enhanced fluxes of upgoing electrons coincident with wave reflection on the Alfven speed gradient above the resonator and from leakage of wave Poynting flux from the resonator region below. These electrons are resonantly accelerated upwards in the upward traveling wave as discussed in section 4.3.

[58] Throughout the interval shown the electron energy flux remains less than the wave Poynting flux at the same altitude except when within the resonator region at $t = 2$ s. Given that only 15.3 erg $cm^{-2}\ s^{-1}$ of wave Poynting flux makes it to the ionosphere, where 76 ergs $cm^{-2}\ s^{-1}$ is estimated from the electron simulation, indicates that in an energy conserving simulation the wave amplitudes may be considerably reduced from those obtained for the non-energy conserving simulation performed here. Furthermore, it can be expected that significantly smaller electron energy fluxes would result. Given that these fields should be strongly attenuated, the fact that large wave amplitudes together with large electron fluxes are in fact observed in the resonator region is a strong argument for the operation of the feedback instability.

6. Conclusion

[59] The ionospheric Alfven resonator has been identified in a case study of the polar cap boundary of the auroral oval near midnight. Poynting flux observations and cross-spectral analysis of electric and magnetic field observations indicate that the first four harmonics of the resonator are excited by a single Gaussian shaped Alfvenic pulse from above. The wave amplitudes are observed to decay in time. Simultaneous electron observations show several bursts of dispersed electrons with energies extending above 10 keV with the peak energy of each successive burst decreasing.

[60] One-dimensional MHD simulations including an electron inertial correction for a statistically determined altitude dependent mass density profile can qualitatively reproduce some of the observed features including the waveforms and frequency dependent phase structure, dispersive electron bursts and details of the observed electron distribution function. However, it is shown that even in the case strongly unstable to the ionospheric feedback instability with large field amplitudes inside the resonator the amount of electron acceleration that occurs within the resonator region is small. In fact it is not possible with the electron inertial correction alone to account for the observed electron peak energies from acceleration inside the resonator region. Most of the electron acceleration due to the inertial effect occurs just above resonator altitudes where the downgoing wave reflects on the Alfven speed gradient from above. Here the observed wave parallel electric field as the wave reflects is significantly larger than for a propagating wave in the local approximation and electrons can gain several keV through quasi-static acceleration in the reflecting wave field. For this reason driving the wave externally provides better agreement with the observed electron energy spectra than possible by allowing the system to evolve from an initial disturbance of the ionospheric Alfven resonator unstable to the feedback instability. However, even in the driven case the observed energies are somewhat higher than possible from the electron inertia derived electric field for realistic perpendicular wave field amplitudes and the statistically derived density and composition profiles used.

[61] In summary, if electrons gain significant energy from within the ionospheric Alfven resonator, then this comparison between observations and simulations inside the resonator suggests that the Alfven wave is capable of producing parallel electric fields at ionospheric resonator altitudes larger than that obtained through electron inertial effects in the linear approximation.

[62] **Acknowledgments.** This work was supported by NASA grant NAG5-3596 and the Physics Department at the Chinese University of Hong Kong. Chris Chaston is particularly indebted to Chu Ming Chung for his support and hospitality while completing this work at Chinese University.

[63] Arthur Richmond thanks Marcin Grzesiak and Robert Lysak for their assistance in evaluating this manuscript.

References

Andre, M., and L. Eliasson, Electron acceleration by low frequency electric field fluctuations: Electron conics, *Geophys. Res. Lett.*, *19*, 1073, 1992.

Baron, M. J., Electron densities within auroras and other E-region characteristics, *Radio Sci.*, *9*, 341, 1974.

Belyaev, P. P., T. Bosinger, S. V. Isaev, and J. Kangas, First evidence at high latitude for the ionospheric Alfven resonator, *J. Geophys. Res.*, *104*, 4305, 1999.

Boehm, M. H., C. W. Carlson, J. P. McFadden, J. H. Clemmons, and F. S. Mozer, High resolution sounding rocket observations of large amplitude Alfven waves, *J. Geophys. Res.*, *95*, 12,157, 1990.

Chaston, C. C., C. W. Carlson, W. J. Peria, R. E. Ergun, and J. P. McFadden, FAST observations of inertial Alfven waves in the dayside aurora, *Geophys. Res. Lett.*, *26*, 647, 1999.

Chaston, C. C., C. W. Carlson, R. E. Ergun, and J. P. McFadden, Alfven waves, density cavities and electron acceleration observed from the FAST spacecraft, *Phys. Scr. T*, *84*, 64, 2000.

Chaston, C. C., J. Bonnell, L. M. Peticolas, C. W. Carlson, R. E. Ergun, and J. P. McFadden, Driven Alfven waves and electron acceleration: A FAST case study, *Geophys. Res. Lett.*, *29*(11), XXXX, doi:10.1029/2001GL013842, 2002a.

Chaston, C. C., L. M. Peticolas, J. W. Bonnell, C. W. Carlson, R. E. Ergun, and J. P. McFadden, The widths and brightness of auroral arcs driven by Inertial Alfven waves, *J. Geophys. Res.*, *107*, XXXX, doi:10.1029/2001JA007537, in press, 2002b.

Chust, T., P. Louarn, M. Volwerk, H. de Feraudy, A. Roux, J.-E. Wahlund, and B. Holback, Electric fields with large parallel component observed by Freja spacecraft, *J. Geophys. Res.*, *103*, 215, 1998.

Clark, A. E., and C. E. Seyler, Electron beam formation by small-scale oblique inertial Alfven waves, *J. Geophys. Res.*, *104*, 17,233, 1999.

Ergun, R. E., et al., FAST satellite wave observations in the AKR source region, *Geophys. Res. Lett.*, *25*, 2061, 1998.

Ergun, R. E., C. W. Carlson, J. P. McFadden, F. S. Mozer, and R. J. Strangeway, Parallel electric fields in discrete arcs, *Geophys. Res. Lett*, *27*, 4053, 2000.

Ergun, R. E., Y.-J. Su, L. Andersson, C. W. Carlson, J. P. McFadden, F. S. Mozer, D. L. Newman, M. V. Goldman, and R. J. Strangeway, Direct observation of localized parallel electric fields in a space plasma, *Phys. Rev. Lett.*, *87*, 4, 2001.

Eriksson, S., R. E. Ergun, C. W. Carlson, and W. Peria, The cross-polar potential drop and its correlation to the solar wind, *J. Geophys. Res.*, *105*, 18,639, 2000.

Goertz, C. K., and R. W. Boswell, Magnetosphere-ionosphere coupling, *J. Geophys. Res.*, *84*, 7239, 1979.

Grzesiak, M., Ionospheric Alfven resonator as seen by Freja satellite, *Geophys. Res. Lett.*, *27*, 923, 2000.

Hui, C.-H., and C. E. Seyler, Electron acceleration by Alfven waves in the magnetosphere, *J. Geophys. Res.*, *97*, 3953, 1993.

Kelley, M. C., J. F. Vickrey, C. W. Carlson, and R. Torbert, On the origin and spatial extent of high-latitude F region irregularities, *J. Geophys. Res.*, *87*, 5217, 1982.

Kletzing, C. A., Electron acceleration by kinetic Alfven waves, *J. Geophys. Res.*, *99*, 11,095, 1994.

Kletzing, C. A., and S. Hu, Alfven wave generated electron time dispersion, *Geophys. Res. Lett.*, *28*, 693, 2001.

Knudsen, D. J., M. C. Kelley, and J. F. Vickrey, Alfven waves in the auroral ionosphere: A numerical model compared with measurements, *J. Geophys. Res.*, *97*, 77, 1992.

Lessard, M. R., and D. J. Knudsen, Ionospheric reflection of small-scale Alfven waves, *Geophys. Res. Lett.*, *28*, 3573, 2001.

Louarn, P., J.-E. Wahlund, T. Chust, H. de Feraudy, A. Roux, B. Holback, P. O. Dovner, A. I. Eriksson, and G. Holmgren, Observations of kinetic Alfven waves by the Freja spacecraft, *Geophys. Res. Lett.*, *21*, 1847, 1994.

Lysak, R. L., Coupling of the dynamic ionosphere to auroral flux tubes, *J. Geophys. Res.*, *91*, 7047, 1986.

Lysak, R. L., Theory of auroral zone PiB pulsation spectra, *J. Geophys. Res.*, *93*, 5942, 1988.

Lysak, R. L., Electrodynamic coupling of the magnetosphere and ionosphere, *Space Sci. Rev.*, *52*, 33, 1990.

Lysak, R. L., Feedback instability of the ionospheric resonant cavity, *J. Geophys. Res.*, *96*, 1553, 1991.

Lysak, R. L., and W. Lotko, On the kinetic dispersion relation for shear Alfven waves, *J. Geophys. Res.*, *101*, 5085, 1996.

Lysak, R. L., and Y. Song, Energetics of the ionospheric feedback instability, *J. Geophys. Res.*, *107*(A8), 1160, doi:10.1029/2001JA000308, 2002.

Pokhotelov, O. A., D. Pokhotelov, A. Streltsov, V. Khruschev, and M. Parrot, Dispersive ionospheric Alfven resonator, *J. Geophys. Res.*, *105*, 7737, 2000.

Rees, M. H., Magnetospheric substorm energy dissipation in the atmosphere, *Planet. Space Sci.*, *23*, 1589, 1975.

Spiro, R. W., P. H. Reiff, and L. J. Maher, Precipitating electron energy fluxes and auroral zone conductances: An empirical model, *J. Geophys. Res.*, *87*, 8215, 1982.

Stasiewicz, K., G. Gustaffson, G. Marklund, P.-A. Lindqvist, J. H. Clemmons, and L. Zanetti, Cavity resonators and Alfven resonance cones observed on Freja, *J. Geophys. Res.*, *102*, 2565, 1997.

Stasiewicz, K., et al., Small scale Alfvenic structure in the aurora, *Sp. Sci. Rev.*, *92*, 423, 2000.

Strangeway, R. J., et al., FAST observations of VLF waves in the auroral zone: Evidence of very low plasma densities, *Geophys. Res. Lett.*, *25*, 265, 1998.

Thompson, B. J., and R. L. Lysak, Electron acceleration by inertial Alfven waves, *J. Geophys. Res.*, *101*, 5359, 1996.

Trakhtengertz, V. Y., and A. Y. Feldstein, Turbulent regime of magnetospheric convection, *Geomagn. Aeron.*, *27*, 221, 1987.

Tsunoda, R. T., High-latitude F region irregularities: A review and synthesis, *Rev. Geophys.*, *26*, 719, 1988.

M. Berthomier, J. W. Bonnell, C. W. Carlson, C. C. Chaston, J. P. McFadden, L. M. Peticolas, and I. Roth, Space Sciences Laboratory, University of California, Berkeley, CA 94720, USA. (matthieu@ssl.berkeley.edu; jbonnell@ssl.berkeley.edu; cwc@ssl.berkeley.edu; ccc@ssl.berkeley.edu; mcfadden@ssl.berkeley.edu; lmp@ssl.berkeley.edu; ilan@ssl.berkeley.edu)

R. E. Ergun, Laboratory for Atmospheric and Space Physics, University of Colorado, Boulder, CO 80309, USA. (ree@fast.colorado.edu)

R. J. Strangeway, Institute for Geophysics and Planetary Physics, University of California, Los Angeles, CA 90024, USA. (strange@igpp.ucla.edu)